

Electrically driven octahedral rotations in SrTiO₃ and PbTiO₃

Jiawang Hong* and David Vanderbilt

Department of Physics and Astronomy, Rutgers University, Piscataway, New Jersey 08854-8019, USA

(Received 3 December 2012; published 13 February 2013)

We investigate the oxygen octahedral rotations that occur in two perovskites, SrTiO₃ and PbTiO₃, as a function of applied three-dimensional electric displacement field, allowing us to map out the phase diagram of rotations in both the paraelectric and ferroelectric regions of the polar response. First-principles calculations at fixed electric displacement field are used to extract parameters of a Landau-Devonshire model that is analyzed to identify the phase boundaries between different rotational states. The calculations reveal a rich phase diagram of rotations versus applied field in both SrTiO₃ and PbTiO₃, although the details are quite different in the two cases.

DOI: [10.1103/PhysRevB.87.064104](https://doi.org/10.1103/PhysRevB.87.064104)

PACS number(s): 77.84.-s, 77.90.+k, 71.15.-m

I. INTRODUCTION

Oxygen octahedral rotations can have a significant impact on the behavior of ABO_3 perovskites, affecting electronic, dielectric, ferroelectric, and magnetic properties. For example, the octahedral rotations couple strongly with the magnetic structure in transition-metal perovskites by modifying the metal-oxygen-metal bond angles that are critical to determine the magnetic interactions.^{1,2} In some materials, such as SrTiO₃, the oxygen rotations give rise to a nonpolar antiferrodistortive (AFD) ground state contributing to the suppression of ferroelectric (FE) order.³⁻⁵ However, the recent discovery of rotation-driven improper ferroelectricity in a superlattice⁶ has inspired a search for this type of ferroelectricity in other types of materials.^{1,7-9} Because they can also couple with magnetic properties, octahedra rotations offer a promising approach to the discovery or design of new multiferroic perovskites.^{1,10-13}

In the cubic structure, SrTiO₃ and PbTiO₃ both show an AFD instability at the zone corner (R point) of the Brillouin zone.^{14,15} Following this instability leads to the experimentally observed tetragonal ground state with rotations along the [001] axis for SrTiO₃, while PbTiO₃ prefers rotations along the [111] axis. For PbTiO₃, however, this is not the equilibrium structure; instead, a strong FE instability at Γ out-competes the AFD instability, giving rise to a tetragonal FE ground state without rotations. Nevertheless, the AFD modes provide a potential source of instability in PbTiO₃, as has been predicted for example for surface^{16,17} and interface⁶ geometries. (In SrTiO₃, a weak FE instability at Γ is found in some calculations, depending sensitively on lattice constant and other details. However, experimentally the material just barely avoids this instability, remaining paraelectric down to zero temperature.)

Oxygen octahedral rotations clearly play an important role in these and other perovskites, and they are known to be strongly affected by stress^{12,18,19} and temperature.²⁰ Recently, the effects of electric displacement field on the AFT rotations were investigated in strained PbTiO₃ bulk and SrTiO₃ bulk²¹ and PbTiO₃/SrTiO₃ superlattice,²² with displacement field and rotation axis fixed along [001]. In this paper, we study the phase transition behavior of the AFD modes in SrTiO₃ and PbTiO₃ under three-dimensional constant electric displacement field.

Of course, SrTiO₃ and PbTiO₃ are qualitatively different in that the latter is ferroelectric while the former remains paraelectric down to zero temperature. However, the choice of fixed electric displacement field \mathbf{D} for the boundary conditions

in this study allows us to treat both materials on an equal footing. The situation would have been much more complicated if we had chosen to work at fixed electric field \mathcal{E} , because the energy landscape is multivalued and the paraelectric configuration is unstable at small \mathcal{E} in a ferroelectric material like PbTiO₃. At fixed \mathbf{D} , however, the energy landscape remains single-valued, thus allowing access to the entire electric equation of state for PbTiO₃ as well as SrTiO₃.^{23,24} Indeed, both materials have a large static dielectric constant, so that mapping at fixed \mathbf{D} is qualitatively similar to mapping at fixed \mathbf{P} (all phases at nonzero \mathbf{D} field exhibit an electric polarization). Thus, in our study, the main qualitative difference between SrTiO₃ and PbTiO₃ will be related to the fact that the rotational instability that prefers to develop along a [001] axis in SrTiO₃ instead prefers a [111] axis in PbTiO₃.

The paper is organized as follows. In Sec. II we introduce the Landau-Devonshire model, provide the details of our first-principles calculations, and specify the terminology for symmetries that will be used later. In Sec. III we present the results of the first-principles calculations in one-dimensional \mathbf{D} -field space and discuss the fitting of the model, which is then used to compute the phase diagram of rotational phases in three-dimensional \mathbf{D} space. Finally, Sec. IV contains a summary.

II. PRELIMINARIES

A. Landau-Devonshire model

In order to explore the octahedral-rotation phase diagram in the space of \mathbf{D} fields, the internal energy U has to be calculated and minimized on a three-dimensional mesh of \mathbf{D} values. Near the phase boundaries between different rotational phases, this process would be quite tedious; the first-principles calculations would need to be very carefully converged, and the procedure would become quite time-consuming. We therefore introduce a Landau-Devonshire model to study the phase transitions in this system, with the coefficients in the model being obtained from fitting to our first-principles results on a smaller database of \mathbf{D} values. This model can then be used to locate the phase boundaries efficiently.

As mentioned above, the dominant AFD rotational instabilities for paraelectric SrTiO₃ and PbTiO₃ are both at the R point in the Brillouin zone (corresponding, in the most general case, to the $a^-b^-c^-$ Glazer notation). We therefore focus on these modes here, and define a vector octahedral rotation

$\theta = (\theta_x, \theta_y, \theta_z)$ describing a rotation by angle θ_x around the x axis, etc. (or, more generally, by angle $\theta = |\theta|$ about axis $\hat{\theta}$).

Within our Landau-Devonshire model, then, the internal energy $U_{\text{tot}}(\mathbf{D}, \theta)$ is expanded as a function of displacement field $\mathbf{D} = (D_x, D_y, D_z)$ and octahedral rotations $\theta = (\theta_x, \theta_y, \theta_z)$ as

$$U_{\text{tot}} = U_D + U_\theta + U_{\text{int}} \quad (1)$$

where

$$U_D(\mathbf{D}) = \alpha(D_x^2 + D_y^2 + D_z^2) + \beta(D_x^4 + D_y^4 + D_z^4) + \gamma(D_x^2 D_y^2 + D_x^2 D_z^2 + D_y^2 D_z^2), \quad (2)$$

$$U_\theta(\theta) = \mu(\theta_x^2 + \theta_y^2 + \theta_z^2) + \omega(\theta_x^4 + \theta_y^4 + \theta_z^4) + \sigma(\theta_x^2 \theta_y^2 + \theta_x^2 \theta_z^2 + \theta_y^2 \theta_z^2), \quad (3)$$

$$U_{\text{int}}(\mathbf{D}, \theta) = \tau(\theta_x^2 D_x^2 + \theta_y^2 D_y^2 + \theta_z^2 D_z^2) + \lambda(\theta_x^2 D_y^2 + \theta_x^2 D_z^2 + \theta_y^2 D_x^2 + \theta_y^2 D_z^2 + \theta_z^2 D_x^2 + \theta_z^2 D_y^2) + \kappa(\theta_x \theta_y D_x D_y + \theta_x \theta_z D_x D_z + \theta_y \theta_z D_y D_z). \quad (4)$$

Here we have made the approximation of truncating the expansion systematically at overall fourth order, and $\alpha, \beta, \gamma, \mu, \omega, \sigma, \tau, \lambda,$ and κ are coefficients that need to be fitted from the first-principles calculations. The terms in U_{int} describe the coupling of \mathbf{D} and octahedral rotations. There is no strain in this expansion since each term is defined assuming that the strain is fully relaxed for each (\mathbf{D}, θ) value.

In the present work we are really only interested in the internal energy difference $U_{\text{tot}}(\mathbf{D}, \theta) - U_{\text{tot}}(\mathbf{D}, 0)$ between the states with and without octahedral rotations. We denote this quantity simply as U and note that

$$U(\mathbf{D}, \theta) = U_\theta(\theta) + U_{\text{int}}(\mathbf{D}, \theta). \quad (5)$$

In order to fit the coefficients from first-principles calculations, we first apply \mathbf{D} along just one Cartesian direction, which we choose as D_z , to find the coefficients $\mu, \omega, \sigma, \tau,$ and λ . For this case we set $D_x = D_y = 0$ and find

$$U = \mu\theta^2 + \tau D_z^2 \theta_z^2 + \lambda D_z^2 (\theta_x^2 + \theta_y^2) + \omega\theta^4 + (\sigma - 2\omega)(\theta_x^2 \theta_y^2 + \theta_x^2 \theta_z^2 + \theta_y^2 \theta_z^2). \quad (6)$$

We then do a series of calculations in which we choose different initial structures with equilibrium rotations along $\hat{\theta} = [100], [110], [001],$ or $[111]$ at $D_z = 0.0$ a.u., and for each choice (and for each D_z) we relax all the coordinates to obtain the internal energy $U(D_z, \hat{\theta})$. (We increase D_z in increments of 0.04 a.u. up to 0.12 a.u. for SrTiO₃, and increments of 0.02 a.u. up to 0.08 a.u. for PbTiO₃.) Fitting the model parameters to this first-principles database of information, we obtain all the coefficients in Eqs. (3) and (4) except for κ . We then do one more series of calculations with both \mathbf{D} and θ along the $[111]$ direction, i.e., $\mathbf{D} = (D_0, D_0, D_0)$ and $\theta = (\theta_0, \theta_0, \theta_0)$, for which the model predicts

$$U = 3\mu\theta_0^2 + 3(\omega + \sigma)\theta_0^4 + 3(\tau + \kappa + 2\lambda)\mathbf{D}_0^2\theta_0^2. \quad (7)$$

(Here D_z is increased in steps of 0.02 a.u. up to 0.08 a.u. for both materials.) Fitting in a similar way to these results, we obtain the parameter κ as well. Once all the parameters are in hand, we can go back to Eq. (5) and study the full behavior

of octahedral rotations as a function of three-dimensional \mathbf{D} space using this model.

B. First-principles methodology

Our calculations were performed within density-functional theory in the local-density approximation²⁵ using norm-conserving pseudopotentials²⁶ and a plane-wave cutoff of 60 Ha. A $6 \times 6 \times 6$ Monkhorst-Pack grid²⁷ was used to sample the Brillouin zone. The unit cell for simulating the R -point rotation is doubled to obtain a 10-atom fcc cell. The atomic coordinates and lattice vectors of this cell were relaxed until all atomic force components were smaller than 10^{-5} Ha/Bohr and all stress components were below 10^{-7} Ha/Bohr³. We used the open-source ABINIT code package²⁸ with the implementation of the constant-displacement-field method in three dimensions²⁴ to calculate the internal energy at a each specified \mathbf{D} field.

C. Terminology for symmetries

Here we introduce the notations that we will use for describing rotational phases, following a scheme similar to the one often used for polarization.²⁹ When the octahedral rotation axis is constrained to a symmetry axis lying along $\langle 001 \rangle, \langle 111 \rangle,$ or $\langle 011 \rangle,$ the resulting phase becomes tetragonal (\mathcal{T}), rhombohedral (\mathcal{R}), or orthorhombic (\mathcal{O}), respectively.³⁰ Similarly, the \mathcal{M} phases arise when rotation axis is confined to a mirror plane. There are three cases: \mathcal{M}_C , in which the axis is along $[0, u, v]$; and \mathcal{M}_A or \mathcal{M}_B , in which the axis is along $[uvw]$ with $u < v$ or $u > v$, respectively. The triclinic phase (Tri) occurs if the axis is along $[uvw]$ with $u \neq v \neq w \neq 0$. We also introduce the Cartesian subscript $\alpha = \{x, y, z\}$ to specify the unique Cartesian direction when needed. For example, \mathcal{T}_α denotes the tetragonal phase with rotation axis along direction α , while \mathcal{O}_α and $\mathcal{M}_{C\alpha}$ denote the orthorhombic phase and \mathcal{M}_C phases with rotation axis lying in the plane perpendicular to the α direction. Similarly, $\mathcal{M}_{A\alpha}$ and $\mathcal{M}_{B\alpha}$ are the \mathcal{M}_A and \mathcal{M}_B phases with the nonequal component v in $[uvw]$ along the α direction.

III. RESULTS

A. First-principles calculations

We first carry out a series of calculations, starting from $\mathbf{D} = 0$ and increasing D_z in steps of 0.04 a.u. for SrTiO₃ and 0.02 a.u. for PbTiO₃, to explore the resulting behavior for the case that the octahedral rotation is constrained to lie along the $[100], [110],$ or $[001]$ axis. At each D_z , the structure is fully relaxed with respect to both ionic positions and lattice parameters. In all three cases in both materials, the rotations, which are fully developed at $D_z = 0$, are gradually suppressed with increasing D_z until they disappear completely at a critical value of D_z . We also attempt this procedure for the case that the octahedral rotations started along the $[111]$ direction at $\mathbf{D} = 0$. However, for SrTiO₃ a rotation along $[111]$ is a saddle point, rather than a local minimum, of the $\mathbf{D} = 0$ energy landscape, and the breaking of the threefold symmetry about $[111]$ by the applied D_z immediately causes the rotation axis to switch to either the $[110]$ or $[001]$ direction. For PbTiO₃, by contrast, the

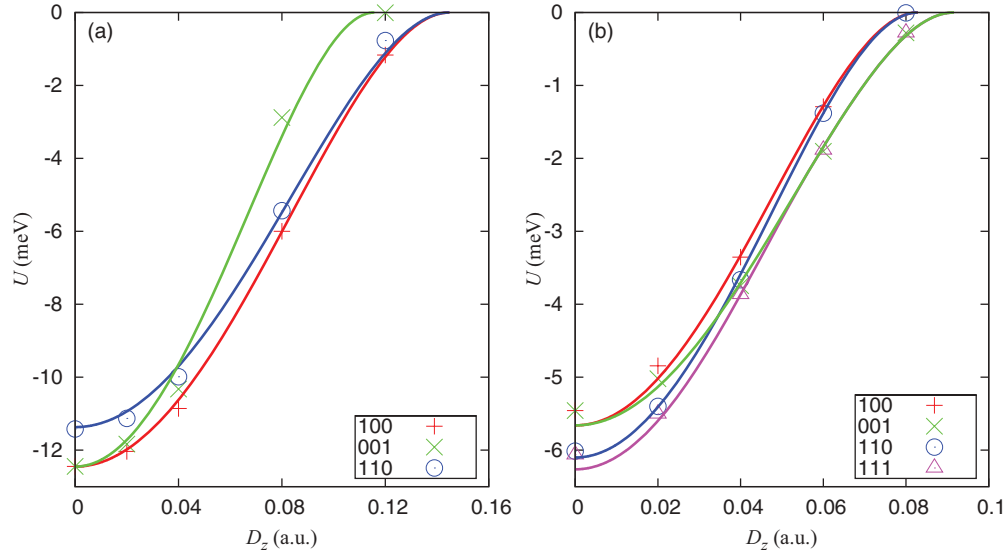


FIG. 1. (Color online) Internal energy U of Eq. (5) for \mathbf{D} applied along the \hat{z} direction, for phases with the octahedral rotations constrained to be about different axes as indicated in the legend. (a) SrTiO₃; (b) PbTiO₃. Symbols are from first-principles calculations; curves are from the Landau-Devonshire model.

$\mathbf{D} = 0$ system has its minimum-energy AFD axis along [111], and we can also follow the evolution of this fourth case as D_z is applied. In this case we find that θ_z gradually increases, and

$\theta_x = \theta_y$ gradually decrease, with increasing D_z , until a critical value is reached at which θ_x and θ_y vanish and the solution merges with the one with the rotation axis constrained to [001]. The results of these calculations are shown as the symbols in Figs. 1 and 2, where the internal energy difference U of Eq. (5) and the equilibrium rotation angles are plotted versus D_z .

We also carry out calculations for both materials with \mathbf{D} and the rotation axis both constrained to lie along [111]. As mentioned in Sec. II A, the purpose of this is just to obtain the additional coefficient κ that was not determined from the calculations with \mathbf{D} along [001], so it was not necessary to study other rotation axes for this case. The results (not shown) again indicate that the rotations gradually decrease with increase of D_0 for $\mathbf{D} = (D_0, D_0, D_0)$, although in the case of SrTiO₃ the rotations never vanish over the range of D_0 up to 0.10 a.u. studied here.

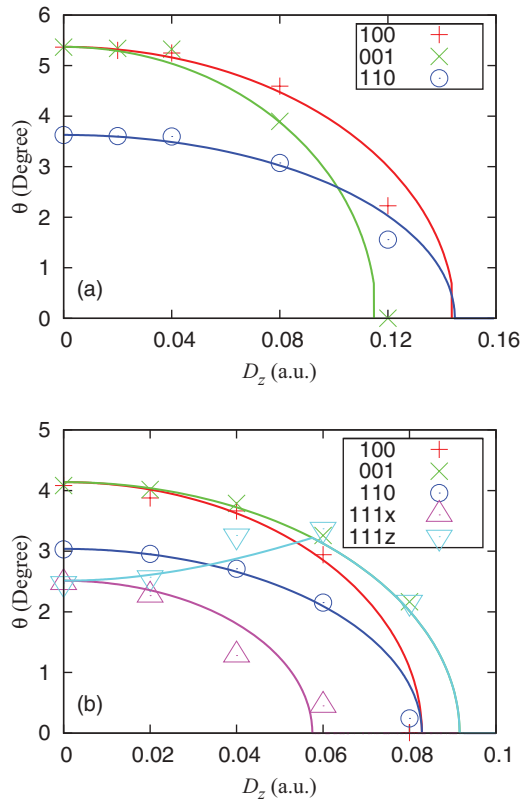


FIG. 2. (Color online) Octahedral rotation angles ($\theta_x, \theta_y, \theta_z$) for different phases for \mathbf{D} applied along \hat{z} . (a) SrTiO₃; (b) PbTiO₃. For [110] cases ($\theta_x = \theta_y$), θ_x is plotted. For the PbTiO₃ [111]-derived case ($\theta_x = \theta_y \neq \theta_z$), θ_x and θ_z are plotted. Symbols are from first-principles calculations; curves are from the model.

B. Fitting of the model parameters

We now use the results of the above first-principles calculations to determine the parameters in Eqs. (3) and (4) following the procedure detailed at the end of Sec. II A. The resulting parameter values are reported in Table I. The predictions of the fit (solid curves) are compared with the direct first-principles results (symbols) in Figs. 1 and 2. It is clear that the model agrees quite well with the first-principles calculations.

TABLE I. Fitted coefficients of the Landau-Devonshire model of Eqs. (3)–(5), defined with energies in meV, rotation angles in degrees, and displacement fields in a.u..

	μ	ω	σ	τ	λ	κ
SrTiO ₃	-0.863	0.015	0.036	64.45	41.19	-139.36
PbTiO ₃	-0.661	0.019	0.033	78.80	96.27	-147.91

C. Details for \mathbf{D} along [001]

From Fig. 1, we can see that SrTiO_3 and PbTiO_3 have different octahedral rotation patterns. At $\mathbf{D} = 0$, SrTiO_3 has the lowest energy in the \mathcal{T} phase, which is its true ground state experimentally below 105 K, and the highest energy in the \mathcal{R} phase (not shown in the figure because it is destabilized by any finite D_z). In PbTiO_3 , on the other hand, the energy ordering is just the opposite, with the \mathcal{R} phase lowest and the \mathcal{T} phase highest in energy. In the context of Eq. (6), the energy ordering of the phases at $\mathbf{D} = 0$ is determined by the combination of parameters $(\sigma - 2\omega)$, with the \mathcal{R} or \mathcal{T} phase lowest in energy when this combination is negative or positive, respectively. This is confirmed by the coefficients in Table I.

As D_z increases, Fig. 1 shows that the internal energy U of SrTiO_3 and PbTiO_3 increases and finally reaches zero. Recalling that U is measured relative to the structure with no rotations, we conclude that the octahedral rotations disappear at a sufficiently high D_z field. However, the behavior is different for these two materials. Fig. 1(a) shows that for SrTiO_3 the \mathcal{T} phase³⁰ with rotation axis along [100] or [010] has the lowest energy as D_z increases, which is consistent with recent experiment observation.³¹ While the \mathcal{T} phase with rotation along [001] increases sharply in energy and becomes the least favorable state when $D_z > 0.05$ a.u.. This suggests that the \mathcal{T} phase with its rotation axis perpendicular to \mathbf{D} is suppressed less than the rotation axis parallel to \mathbf{D} . However, PbTiO_3 has a quite different behavior, as can be seen in Fig. 1(b). The state of lowest internal energy at $\mathbf{D} = 0$ is the \mathcal{R} phase. As D_z increases, the rotational axis is perturbed to be along $[uvv]$ for $v > u$, putting the system in the \mathcal{M}_A phase. Eventually, the internal energy of this state merges into the curve for the \mathcal{T} phase (axis along [001]), indicating a phase transition from \mathcal{M}_A to \mathcal{T} at some critical value of D_z . The \mathcal{T} phase, with its rotation axis parallel to D , is then favored at higher D_z , until there is a second phase transition at which the rotations disappear.

The details of the rotational behavior in PbTiO_3 can be seen more clearly in Fig. 2(b), which shows the variation of the various rotation angles with D_z field. The rotation angles decrease as D_z increases for all phases except for the initial \mathcal{R} phase. This phase is immediately perturbed to become \mathcal{M}_A as soon as a nonzero D_z is present. With increasing D_z , the rotation angles θ_x and θ_y decrease, but θ_z increases. That is, the rotation axis starts from [111] (\mathcal{R}) and then rotates in the $(1\bar{1}0)$ plane (\mathcal{M}_A) towards [001] (\mathcal{T}). We can now see that the critical D_z at which \mathcal{T} phase is reached (i.e., at which θ_x and θ_y vanish) is at $D_z = 0.058$ a.u. This also corresponds to the merger of \mathcal{M}_A and \mathcal{T} phases in the internal energy curves of Fig. 1(b). For larger D_z , θ_z then decreases monotonically and reaches zero at $D_z = 0.092$ a.u..

For SrTiO_3 , on the other hand, the picture is simpler. As D_z increases in Fig. 2(a), the rotation axis remains along [100] while the amplitude of θ_x monotonically decreases and disappears entirely at a critical value of $D_z = 0.144$ a.u..³²

D. Three-dimensional \mathbf{D} field

We now turn to a detailed discussion of the behavior of SrTiO_3 and PbTiO_3 as a function of three-dimensional \mathbf{D} field,

based on the model of Eqs. (3)–(5) using the coefficients fitted from first principles as reported in Table I.

First, note that because the coefficient μ is negative in both SrTiO_3 and PbTiO_3 , we are guaranteed to get a phase with nonzero rotations at small D . Also, because of the non-zero value of κ , we generically obtain a triclinic rotational axis ($\theta_x \neq \theta_y \neq \theta_z$) at a general point $D_x \neq D_y \neq D_z \neq 0$ in \mathbf{D} space. High-symmetry phases will only exist under special conditions, i.e., when one or more \mathbf{D} components vanish, or when two or more \mathbf{D} components are equal.

1. Phase diagram for SrTiO_3

Figure 3 shows several two-dimensional (D_x, D_y) slices of the three-dimensional phase diagram of STO taken at different values of D_z . In these panels, the outer solid (blue) boundaries [and also the inner ones in Fig. 3(d) and 3(e)] indicate a second-order phase transition from a phase with octahedral rotations to a phase without rotations. Other solid lines represent first-order phase boundaries as will be explained below. Dashed and dotted lines are not true phase boundaries, but instead denote high-symmetry structures that occur as special cases along special lines or planes in \mathbf{D} space; we use dashed lines (red) for \mathcal{M}_A or \mathcal{M}_B phases, dotted lines (black) for \mathcal{T} phases, dashed-dotted lines (green) for \mathcal{M}_C phases, and short-dashed-dotted lines (brown) for \mathcal{O} phases, using the notation developed in Sec. II C.

In Fig. 3(a), for $D_z = 0$, the squarish solid curve marked by crosses (green) is a first-order boundary separating the \mathcal{T}_z phase (inside) from phases with $\theta_z = 0$ (outside). For generic (D_x, D_y) outside, this corresponds to the \mathcal{M}_{Cz} phase (recall, from Sec. II C, that this means that the rotation axis lies in the θ_x - θ_y plane). Along the horizontal axis ($D_y = 0$) outside, shown by the dotted (black) line, the \mathcal{T}_z and \mathcal{T}_y phases are degenerate. However, any small finite D_y favors the \mathcal{T}_y phase and adds a small θ_x component (via the κ term) so that the \mathcal{M}_{Cz} phase results. That is, crossing this dotted line from negative to positive D_y just causes θ_x to cross smoothly through zero, so that this is not a true phase boundary.

Along the [110] direction in \mathbf{D} space, the behavior is rather complex. We let $D_x = D_y = D_0$. Recall that inside the square region (small D_0) one finds the \mathcal{T}_z phase. Next comes a segment of first-order phase boundary, indicated again by a solid line with crosses (green), along which there are two degenerate \mathcal{M}_{Cz} phases with rotation angles $(\theta_a, \theta_b, 0)$ and $(\theta_b, \theta_a, 0)$ (with $\theta_a \neq \theta_b$). Any small step away from this line (while remaining in the $D_z = 0$ plane) favors one or the other of these phases, and also slightly perturbs its angles θ_x and θ_y . Thus, when crossing this line, both θ_x and θ_y jump discontinuously. When D_0 increases further, as shown by the dash-dotted (brown) line, one finds the \mathcal{O}_z phase exactly on this line, but it is just a special case of the \mathcal{M}_{Cz} phase as $|\theta_x|$ and $|\theta_y|$ cross smoothly through each other. Like the dotted (black) line, therefore, this is not a true phase boundary.

As D_z increases from zero, the behavior of the phase diagram is initially very complex, especially in the vicinity of the squarish central region of Fig. 3(b). The phase behavior in the outer region at $D_z = 0.015$ a.u. is shown in Fig. 3(b). The \mathcal{M}_{Cz} phase at $D_z = 0$ is perturbed to become triclinic as θ_z becomes nonzero linearly in D_z . The \mathcal{T}_x and \mathcal{T}_y lines at $D_z = 0$ are perturbed to \mathcal{M}_C structures as shown by the dash-dotted

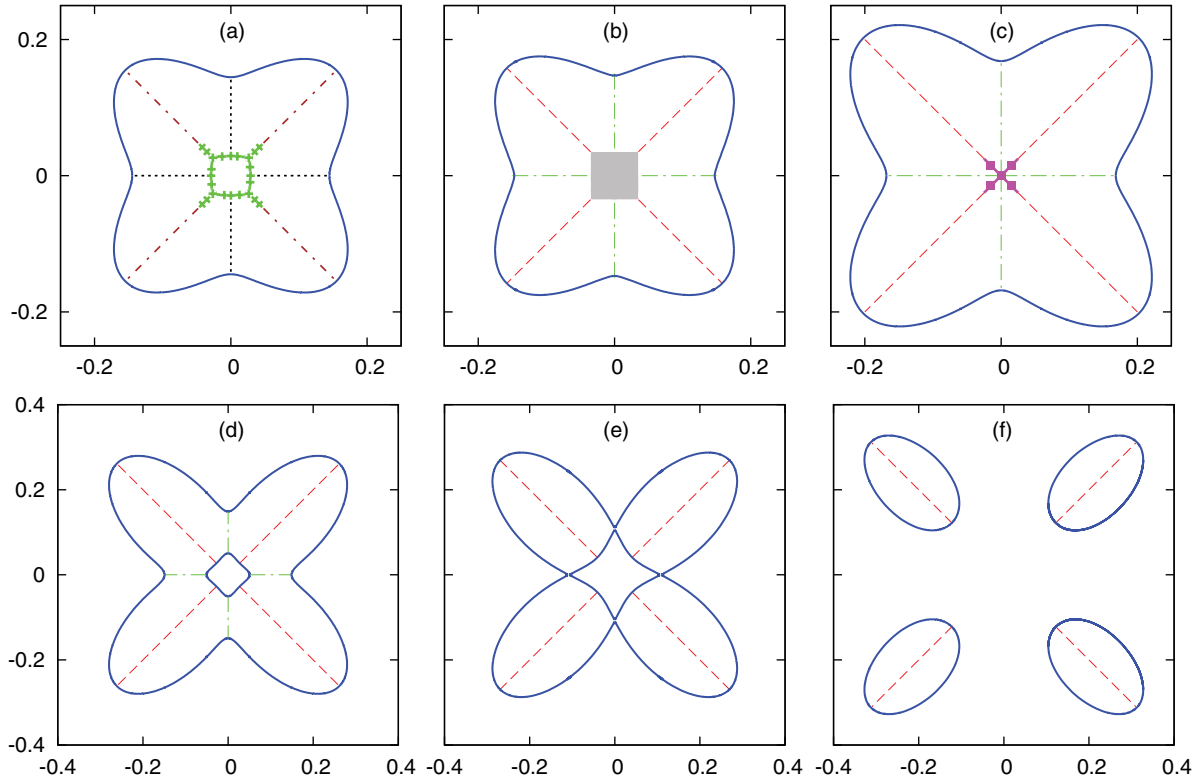


FIG. 3. (Color online) Phase diagram for rotational phases of SrTiO₃ under applied \mathbf{D} field. Each panel is a cut plotted in the D_x - D_y plane (note the change of scale between top and bottom panels) at fixed D_z . (a) $D_z = 0.00$ a.u.; (b) 0.015 a.u.; (c) 0.08 a.u.; (d) 0.16 a.u.; (e) 0.172 a.u.; (f) 0.24 a.u.. Solid lines are second-order boundaries; decorated solid lines are first-order boundaries; and dashed, dash-dotted, and dotted lines are special cases of higher symmetry induced by high-symmetry \mathbf{D} vectors (see text for details). Gray area in (b) is detailed in Fig. 4.

(green) lines, and the \mathcal{O}_z lines are converted to \mathcal{M}_A and \mathcal{M}_B structures as shown by the dashed (red) lines. There are no true phase transitions when crossing these nonsolid lines.

The phase behavior in the inner (grayed-out region) of Fig. 3(b) is sufficiently complicated that we chose to provide a separate Fig. 4 to describe the behavior there. The six panels of Fig. 4 show a blow-up of the phase diagram in the range $D_z \in [0, 0.05]$ a.u., with color coding as explained in the caption. We shall not describe all the details here, as these delicate transitions occur in quite a small region around the origin in \mathbf{D} space and are not very relevant to the broader discussion.

In Figs. 3(a)–3(d), the solid outer boundary (second-order transition to the rotationless phase) expands to larger D_x and D_y with increasing D_z (note the change of scale from the first three to the last three panels). In Fig. 3(c), which is for $D_z = 0.08$ a.u., the first-order boundaries, shown by solid lines marked by squares (magenta), are the remnant of the first-order boundaries of Figs. 4(e) and 4(f); these diminish and disappear as D_z is increased further. Then, by the time $D_z = 0.16$ a.u. is reached in Fig. 3(d), a new pocket of rotationless phase appears near the origin in the D_x - D_y plane. This pocket grows until, at a critical value of $D_z = 0.172$ a.u. shown in Fig. 3(e), the inner and outer regions connect and split the region of rotational phases into four ellipses, as shown for $D_z = 0.24$ a.u. in Fig. 3(f). We expected these ellipses to shrink and disappear with a further increase of D_z , but in fact this happens only very slowly; along the line $D_x = D_y = D_z$, the rotations survive to quite large values of \mathbf{D} , as is confirmed by the first-principles

calculations upon which the model is based. We comment on this further in Sec. III E.

2. Phase diagram for PbTiO₃

The situation is simpler for the rotational phase diagram of PbTiO₃. The phase diagrams for several snapshots at increasing D_z are shown in Fig. 5 for PbTiO₃ using the same conventions as in Fig. 3 wherever possible. When $D_z = 0$ as in Fig. 5(a), the center point ($\mathbf{D} = 0$) is in the \mathcal{R} phase. The surrounding area enclosed by the solid lines (green) is triclinic except along the [100] and [110] symmetry lines, which are \mathcal{M}_{Ax} (lines with circles, red) and \mathcal{M}_{Bz} (dashed lines, red) respectively. The transition is continuous across the latter, but first order across the former. Essentially, at small three-dimensional \mathbf{D} , the system prefers to be in a slightly perturbed version of one of four \mathcal{R} phases, depending on the octant in which \mathbf{D} resides. Using the notation \mathcal{S}_{+++} to denote the octant with $D_x > 0$, $D_y > 0$, $D_z < 0$, etc., we find that the \mathcal{R} -like phase with $\hat{\theta} \simeq [111]$ is preferred in \mathcal{S}_{+++} and \mathcal{S}_{---} ; $\hat{\theta} \simeq [\bar{1}11]$ is preferred in \mathcal{S}_{-++} and \mathcal{S}_{+--} ; $\hat{\theta} \simeq [1\bar{1}1]$ is preferred in \mathcal{S}_{+-+} and \mathcal{S}_{-+-} ; and $\hat{\theta} \simeq [11\bar{1}]$ is preferred in \mathcal{S}_{++-} and \mathcal{S}_{--+} . The planes $D_x = 0$, $D_y = 0$, and $D_z = 0$ thus form first-order boundaries in this small- \mathbf{D} region, appearing as solid lines (labeled with circles, red) in the 2D plots. It follows that the octahedral rotation can be “switched” between these \mathcal{R} -like (actually, triclinic) phases by a small change of external electric displacement field.

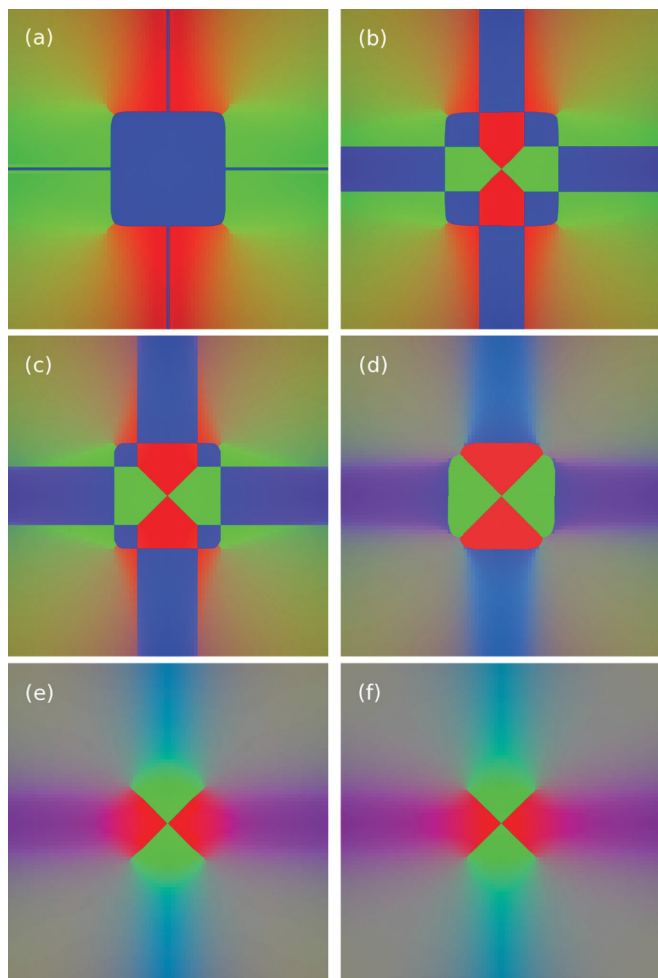


FIG. 4. (Color online) Enlargement of the central portion of Fig. 3 ($D_x, D_y \in [-0.08, 0.08]$ a.u.) for small D_z values. (a) $D_z = 0.00$ a.u.; (b) 0.01 a.u.; (c) 0.015 a.u.; (d) 0.025 a.u.; (e) 0.04 a.u.; (f) 0.05 a.u.. Color coding is such that pure red, green, and blue correspond to the T_x , T_y , and T_z phases respectively, with color values weighted according to $|\theta_x|$, $|\theta_y|$, and $|\theta_z|$ for intermediate phases.

The area between the inner (green) and outer (blue) solid lines in Fig. 5(a) is the \mathcal{M}_{C_z} phase, which becomes \mathcal{O}_z along [110] directions (short-dashed-dotted lines, brown) and T_x along [100] direction (dotted lines, black). The inner solid

(green) lines thus represent second-order phase boundaries at which $\theta_z \rightarrow 0$ as one passes to the outside.

As was the case for SrTiO_3 , the high-symmetry phases for PTO in Fig. 5(a) become lower-symmetry phases as D_z increases, Figs. 5(b) and 5(c). In fact, as soon as $D_z > 0$, the entire region inside the solid (blue) boundary is generically triclinic. Special cases occur along the dashed lines (red), where the symmetry is \mathcal{M}_A or \mathcal{M}_B , and along the dashed-dotted lines (green), which is \mathcal{M}_C . When D_z is small enough, as in Fig. 5(b), the first-order phase boundaries mentioned above are still visible as the solid lines with squares (magenta) near the origin, corresponding to the \mathcal{O}_z phase, but with increasing D_z these shrink and then vanish, as shown in Fig. 5(c). The solid (blue) boundary, outside which the rotational phases disappear, can also be seen to shrink with increasing D_z , at first slowly and then more rapidly, and to disappear by the time D_z reaches 0.10 a.u..

E. Discussion

There are quite significant differences between the rotational phase diagrams for SrTiO_3 and PbTiO_3 , as shown in Figs. 3 and 5. At small \mathbf{D} , the major differences arise from the fact that the $\mathbf{D} = 0$ ground states are different, namely \mathcal{T} and \mathcal{R} respectively. Thus, small applied \mathbf{D} fields essentially switch the system between \mathcal{T} -like phases in SrTiO_3 , or between \mathcal{R} -like phases in PbTiO_3 .

As \mathbf{D} gets larger, the behavior becomes rather complex, but we can identify an important difference that can be traced back to the parameter values of the model. Namely, we notice a much more isotropic behavior of the outer boundary at which the rotations disappear in PbTiO_3 compared to SrTiO_3 . In PbTiO_3 , for example, we find that the critical magnitude of D at which the rotations disappear is ~ 0.09 a.u. and ~ 0.07 a.u. in the [100] and [111] \mathbf{D} -space directions respectively. For SrTiO_3 , on the other hand, the corresponding values are ~ 0.14 and ~ 0.40 a.u. respectively. In addition to being larger (reflecting the stronger tendency to rotational instability in SrTiO_3), the anisotropy between [100] and [111] directions in \mathbf{D} space along the [111] direction. This can be understood from the coefficients reported in Table I. Restricting ourselves to the case of $\mathbf{D} = (D_0, D_0, D_0)$ and $\boldsymbol{\theta} = (\theta_0, \theta_0, \theta_0)$, the

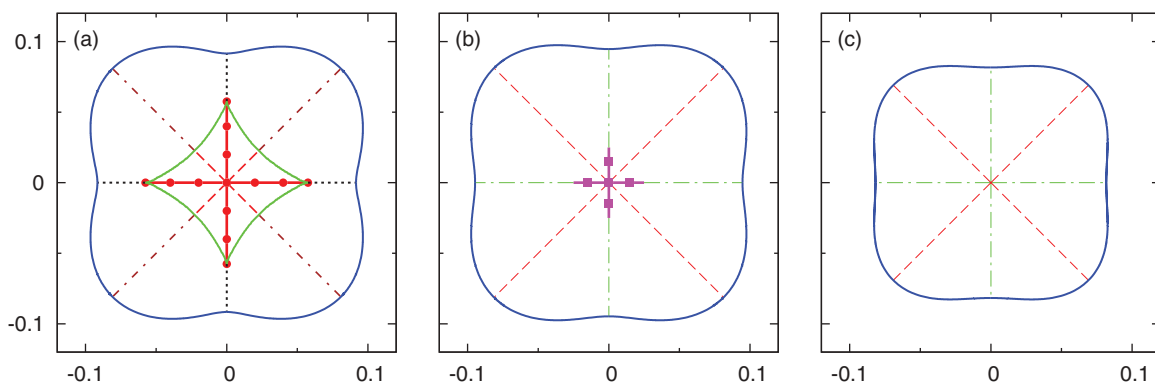


FIG. 5. (Color online) Phase diagram for rotational phases of PbTiO_3 under applied \mathbf{D} field. D_x - D_y are cuts plotted at (a) $D_z = 0.00$ a.u.; (b) 0.02 a.u.; (c) 0.08 a.u.. Conventions are similar to those of Fig. 3 (see text for details).

critical displacement D_c can be obtained from Eq. (5) as $D_c^2 = -\mu/(\tau + 2\lambda + \kappa)$. From this we obtain $D_c = 0.34$ and 0.07 a.u. for SrTiO₃ and PbTiO₃ respectively. The greatly enhanced anisotropy and large value of D_c along this [111] direction can thus be traced to the small value of the denominator $(\tau + 2\lambda + \kappa)$ for SrTiO₃.

It is useful to put the above results in perspective regarding the dielectric behavior. SrTiO₃ is known experimentally to remain paraelectric down to 0 K, so that the entire space of \mathbf{D} fields should be accessible by varying an applied \mathcal{E} field, even if the dielectric constant is very large. PbTiO₃, on the other hand, is strongly ferroelectric, so that the region of small \mathbf{D} corresponds physically to the saddle point of the multiwell energy landscape. This internal-energy landscaped as a function of \mathbf{D} (without octahedral rotations) was mapped out in our previous work,²⁴ where the spontaneously polarized tetragonal ground state occurs at $|D_{[001]}| = 0.17$ a.u.. Similarly, the spontaneously polarized states with constrained orthorhombic and rhombohedral symmetry occur at $|D_{[110]}| = 0.15$ a.u. and $|D_{[111]}| = 0.14$ a.u. respectively. So, we can roughly think of this as a three-dimensional “sombbrero” potential with a radius of ~ 0.15 a.u.. In comparison, the results presented above show that the octahedra rotations disappear for $|D_z| > 0.09$ a.u. and $|D_{[110]}| > 0.11$ a.u.. Thus, the entire region of the interesting rotational phase diagram shown in Fig. 5 lies inside the sombrero radius, in the region where the crystal is unstable under fixed \mathcal{E} (but not under fixed \mathbf{D}) electric boundary conditions.

IV. SUMMARY AND CONCLUSION

In summary, we have investigated the phase transitions associated with oxygen octahedral rotations in SrTiO₃ and PbTiO₃ as a function of a three-dimensional applied electric displacement field, first directly from first-principles calculations and then also using a fitted Landau-Devonshire model. For SrTiO₃, the $\mathbf{D} = 0$ ground state is tetragonal,

with degenerate states corresponding to the rotation angle lying along one of the three Cartesian axes, and for small \mathbf{D} vectors the ground state is a weakly perturbed version of one of these states. Similarly, for PbTiO₃, the $\mathbf{D} = 0$ ground state is rhombohedral, with four degenerate states having rotation axis in one of the [111] or related directions, and again a small \mathbf{D} selects and weakly perturbs one of these states. However, as the strength of \mathbf{D} is increased, we find a quite complicated phase diagram for each material, with both first- and second-order phase boundaries appearing in different parts of the diagram. The structure is especially rich for the case of SrTiO₃. For both materials, the general state associated with generic $D_x \neq D_y \neq D_z \neq 0$ is triclinic, but states with higher symmetry tend to arise when \mathbf{D} itself has higher symmetry. In both materials, the rotations eventually disappear at sufficiently large values of applied \mathbf{D} .

Our work represents one of the first attempts to carry out a systematic three-dimensional characterization of the interplay between polar and octahedral-rotation degrees of freedom in perovskites of this class. There is no external field that couples directly to the rotational degrees of freedom in the same sense that the electric field couples to polarization, so that is difficult to find ways of controlling the rotations directly. However, the present work demonstrates that, once rotations occur spontaneously, their magnitudes can be modified and their orientations can be switched via the application of appropriate electric fields. In any case, the observed richness of behavior suggests that there may be much more to learn in other materials of this class and in more distantly related materials.

ACKNOWLEDGMENTS

This work was supported by ONR Grant No. N-00014-05-1-0054. Computations were done at the Center for Piezoelectrics by Design.

*hongjw10@physics.rutgers.edu

¹N. A. Benedek and C. J. Fennie, *Phys. Rev. Lett.* **106**, 107204 (2011).

²J. Hong, A. Stroppa, J. Íñiguez, S. Picozzi, and D. Vanderbilt, *Phys. Rev. B* **85**, 054417 (2012).

³W. Zhong and D. Vanderbilt, *Phys. Rev. Lett.* **74**, 2587 (1995).

⁴N. Sai and D. Vanderbilt, *Phys. Rev. B* **62**, 13942 (2000).

⁵C.-J. Eklund, C. J. Fennie, and K. M. Rabe, *Phys. Rev. B* **79**, 220101 (2009).

⁶E. Bousquet, M. Dawber, N. Stucki, C. Lichtensteiger, P. Hermet, S. Gariglio, J. Triscone, and P. Ghosez, *Nature (London)* **452**, 732 (2008).

⁷T. Fukushima, A. Stroppa, S. Picozzi, and J. M. Perez-Mato, *Phys. Chem. Chem. Phys.* **13**, 12186 (2011).

⁸J. López-Pérez and J. Íñiguez, *Phys. Rev. B* **84**, 075121 (2011).

⁹C. Ederer and N. A. Spaldin, *Phys. Rev. B* **74**, 024102 (2006).

¹⁰G. Lawes, *Physics* **4**, 18 (2011).

¹¹N. A. Benedek, A. T. Mulder, and C. J. Fennie, *J. Solid State Chem.* **195**, 11 (2012).

¹²J. M. Rondinelli and N. A. Spaldin, *Adv. Mater.* **23**, 3363 (2011).

¹³J. M. Rondinelli and C. J. Fennie, *Adv. Mater.* **24**, 1961 (2012).

¹⁴Ph. Ghosez, E. Cockayne, U. V. Waghmare, and K. M. Rabe, *Phys. Rev. B* **60**, 836 (1999).

¹⁵Ph. Ghosez, D. Desquesnes, X. Gonze, and K. M. Rabe, in *Fundamental Physics of Ferroelectrics 2000*, edited by R. E. Cohen, AIP Conf. Proc. No. 535 (AIP, Woodbury, New York, 2000), pp. 102–110.

¹⁶A. Munkholm, S. K. Streiffer, M. V. Ramana Murty, J. A. Eastman, C. Thompson, O. Auciello, L. Thompson, J. F. Moore, and G. B. Stephenson, *Phys. Rev. Lett.* **88**, 016101 (2001).

¹⁷C. Bungaro and K. M. Rabe, *Phys. Rev. B* **71**, 035420 (2005).

¹⁸J. M. Rondinelli and S. Coh, *Phys. Rev. Lett.* **106**, 235502 (2011).

¹⁹S. J. May, J.-W. Kim, J. M. Rondinelli, E. Karapetrova, N. A. Spaldin, A. Bhattacharya, and P. J. Ryan, *Phys. Rev. B* **82**, 014110 (2010).

- ²⁰K. A. Muller, W. Berlinger, and F. Waldner, *Phys. Rev. Lett.* **21**, 814 (1968).
- ²¹C. W. Swartz and X. Wu, *Phys. Rev. B* **85**, 054102 (2012).
- ²²M. Stengel, Craig J. Fennie, and Ph. Ghosez, *Phys. Rev. B* **86**, 094112 (2012).
- ²³M. Stengel, N. A. Spaldin, and D. Vanderbilt, *Nat. Phys.* **5**, 304 (2009).
- ²⁴J. Hong and D. Vanderbilt, *Phys. Rev. B* **84**, 115107 (2011).
- ²⁵J. P. Perdew and Y. Wang, *Phys. Rev. B* **45**, 13244 (1992).
- ²⁶N. Troullier and J. L. Martins, *Phys. Rev. B* **43**, 1993 (1991).
- ²⁷H. J. Monkhorst and J. D. Pack, *Phys. Rev. B* **13**, 5188 (1976).
- ²⁸X. Gonze *et al.*, *Comput. Mater. Sci.* **25**, 478 (2002).
- ²⁹D. Vanderbilt and M. H. Cohen, *Phys. Rev. B* **63**, 094108 (2001).
- ³⁰Note that \mathcal{T} , \mathcal{R} , and \mathcal{O} denote only the symmetry of the octahedral rotation axis. They do not necessarily denote the symmetry of the overall phase, which is determined also by the \mathbf{D} field. Real tetragonal, rhombohedral, and orthorhombic phases are denoted as T , R , and O , respectively, in this paper.
- ³¹J. Sidoruk, J. Leist, H. Gibhardt, M. Meven, K. Hradil, and G. Eckold, *J. Phys.: Condens. Matt.* **22**, 235903 (2010).
- ³²The rotation angle here is $\theta_x = 5.4^\circ$ at $\mathbf{D} = 0$, consistent with previous LDA results.^{21,33–35} In Ref. 35 it was shown that the rotation angle is reduced by $\approx 0.8^\circ$ if quantum zero-point corrections are included. The critical D field (beyond which the rotation disappears) may decrease somewhat if such corrections are taken into account, but we would not expect any qualitative change in the phase diagrams presented here.
- ³³N. Sai and D. Vanderbilt, *Phys. Rev. B* **62**, 13942 (2000).
- ³⁴J. Hong, G. Catalan, J. F. Scott, and E. Artacho, *J. Phys.: Condens. Matt.* **22**, 112201 (2010).
- ³⁵P. Garcia-Fernandez, S. Ghosh, Niall J. English, and J. A. Aramburu, *Phys. Rev. B* **86**, 144107 (2012).